Deep learning-based keypoint detection for electron recoil vertex identification and trajectory reconstruction

Stephanie Paiva-Flynn

Contents

Abstract

Machine learning (ML) techniques that are capable of simultaneously classifying and localizing objects in image data have shown promise in their ability to identify particle tracks with significant spatial overlap. Object detection is one method that is trained to detect tracks with bounding boxes and assign classifications. Recently, the MIGDAL experiment has used object detection in their rare event search for the Migdal effect, which consists of a nuclear recoil (NR) and low energy electron recoil (ER) sharing a vertex. While object detection can detect heavily overlapping ERs and NRs, it does not provide directional information of the tracks, which is crucial for verifying the topological signature of the Migdal effect. We therefore extend on MIGDAL's work by utilizing object keypoint detection, a method that, in addition to detecting tracks, is also trained to identify key points within each detected object. We explore the use of object keypoint detection both for vertex reconstruction and trajectory fitting using a large sample of simulated 5.9 keV ^{55}Fe tracks. We report preliminary results comparing 2D vertex position identification using keypoint detection to previously established non ML-based methods, and share our progress on fitting 2D trajectories of these tracks. Directional reconstruction of ERs is of broad interest to applications beyond the MIGDAL experiment, including X-ray astronomy, astrophysical neutrino observations, $0\nu\beta\beta$ and dark matter searches.

Chapter 1

Introduction

Electron directionality is an important signature for a large number of particle detection experiments in order to verify the physical origin of signals, remove backgrounds, or confirm event topologies. It has broad applications in astrophysical X-ray polarimetry, rare event searches, and directional dark matter detection. Electron recoils (ERs), particularly low energy keV-scale events, undergo random walk-like multiple scattering, and as such, directional information can only be extracted from the beginning of the track. ERs are, in general, the most difficult particle tracks to reconstruct due to multiple scattering. Additionally, ERs ionize relatively little near their production points, making it extremely challenging to reconstruct their vertex positions and initial directions. Optimizing directional ER reconstruction performance is therefore of paramount concern and can be done both algorithmically and with the proper choice of detector technology. In this work, we focus on the former.

Expanding on X-ray polarimetry, it allows for investigation of extreme magnetic and gravitational fields around high-energy sources such as pulsars and active galactic nuclei. Previous methods utilized Bragg diffraction and Compton scattering devices to obtain polarization readings. However, a high degree of polarization and intense source flux were required for measurements. This limited observations to only the brightest source in the X-ray sky, the Crab Nebula. These observations were only possible because of the characteristic polarization of synchrotron emission and intense flux of the Crab Nebula. Further investigations were limited by the lack of purpose-built instruments and strict source requirements [1]. Micropattern gaseous detectors with high resolution readouts, such as gas time projection chambers (TPCs) and Gas Pixel Detectors (GPDs) are capable of achieving excellent angular resolution over a wide range of energies, making them ideal candidates for a variety of directional reconstruction applications.

In late 2021 NASA launched the IXPE satellite, with three GPDs onboard. GPDs were designed and built to determine X-ray photon polarization using the photoelectric effect and operate on a similar principle to gas TPCs. Fig 1.1 illustrates the detection principle of a GPD: An incoming X-ray photon
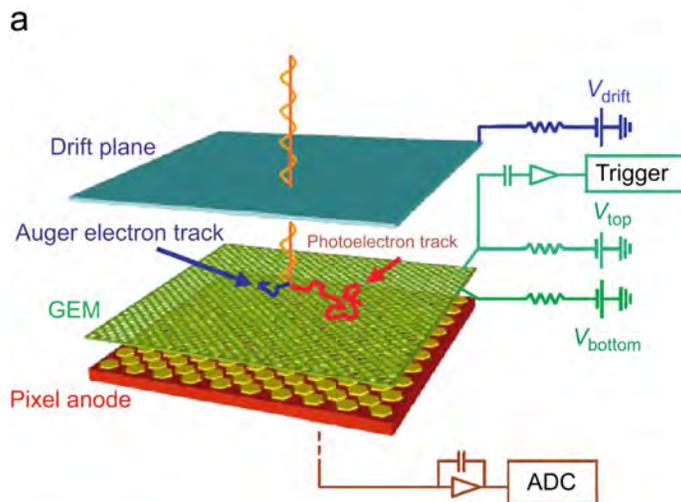
Figure 1.1: GPD used by the IXPE collaboration to detect X-ray polarization

ionizes the gas within the detector, the charge deposited by the subsequent ER then drifts along an electric field. The charge is amplified by a Gaseous Electron Multiplier (GEM), and is finally read out through a pixel anode. It is possible to determine directionality based on the distribution of ionization along the track. Electrons deposit more charge at the end of their tracks, the head, and less at the beginning, the tail. The GPDs employed by IXPE use electron directionality to determine the polarization of X-ray photons. This can be shown by

$$\frac{d\sigma}{d\Omega} \propto \frac{\sin^2\theta\cos^2\phi}{(1 - \beta\cos\theta)^4}, \tag{1.1}$$

which relates the resulting photoelectron direction to the polarization of the ionizing X-ray photon, as shown in Fig 1.2a. β is the electron velocity as a fraction of the speed of light, θ is the polar angle, and ϕ is the azimuthal angle. More specifically, θ is the angle from the xy-plane that the photoelectron is directed. ϕ is the angle in the xy-plane and has a $\cos^2$ relationship with the polarization of the photon. Through this use of electron directionality much broader observations are now possible, offering a new window into the X-ray sky [1][8].

Gas TPCs are particle detectors that allow for full 3D reconstruction of events and multiple readout systems. The example detector to be described here is the TPC used by the MIGDAL collaboration in search of the Migdal effect [6][10]. The MIGDAL detector is an optical TPC that uses low-pressure (50 Torr) gaseous CF_4, Fig 1.3. CF_4 has a high scintillation yield, making it optimal for optical readout. An electric field across the detector causes charge to drift to a double glass GEM system that provides amplification and boosts scintillation. The optical readout is a Hamamatsu ORCA-Quest qCMOS (OQC)
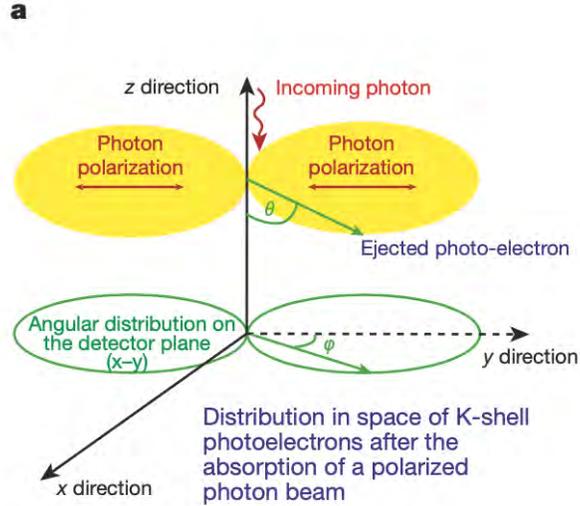
Figure 1.2: Photoelectron direction is proportional to X-ray photon polarization[5].

scientific camera, that was chosen due to its high resolution and quantum efficiency, fast readout speed, and low readout noise. The OQC views the xy projection of the particle tracks. The optical readout system also employs a photomultiplier tube (PMT) that detects primary and secondary scintillation light to determine the initial ionization time. Charge is collected on an Indium Tin Oxide (ITO) anode plate, which has 1D strips along the x-axis and uses timing information to provide the xz projection of the tracks. The OQC, ITO, and PMT in conjunction allow for full 3D event reconstruction [6].

Neutrinoless double beta decay ($0\nu\beta\beta$) searches are another application that can utilize electron directionality for signal confirmation and background rejection. While all $0\nu\beta\beta$ searches rely on extreme radiopurity and excellent energy resolution in their region of interest, experiments such as NEXT use high pressure gaseous Xenon TPCs, enabling them to reconstruct event topologies. The characteristic topology of a double beta decay event is two ERs originating from the same vertex. To verify that an event is from double beta decay, both electrons must be traced to the same location, which vertex reconstruction can assist with. Similarly, for the MIGDAL experiment, the expected topology of the Migdal effect is a nuclear recoil (NR) and an ER that share a vertex. NRs are, in general, higher energy and deposit most of their energy at the tail, as opposed to ERs which deposit a majority of their energy at the head. This can act to obscure the ERs vertex. The ability to reconstruct the ER vertex will allow for verification of the Migdal effect which has yet to be experimentally observed.
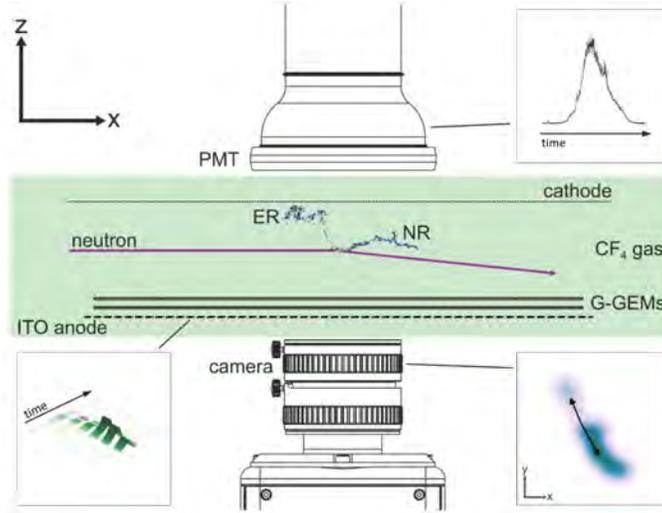
5

Figure 1.3: Diagram of the MIGDAL detector used to search for the Migdal effect.

For the purposes of this work, we define ER trajectory reconstruction to consist of vertex placement and axial angle reconstruction. We aim to quantitatively compare the performance of two methods for these two metrics. The first method of trajectory reconstruction is a novel application of machine learning using the Ultralytics YOLOv8 neural network to make predictions on vertex location and angular orientation. The second method is the re-implementation of an existing analysis algorithm, used by the IXPE collaboration, that is based on mathematical analysis of the moments of the charge distribution.

In addition to ER trajectory reconstruction, work was conducted on a hardware project to develop a high resolution detector to detect the Migdal effect. This detector seeks to probe the low energy regime of the Migdal effect. Chapter 2 will discuss this work, conducted over the summer of 2024 at the Los Alamos Neutron Science Center (LANSCE), which mainly focused on hardware tasks to reduce electronic noise in the detector. The remainder of the thesis describes my work on directional algorithms for ER tracks. Chapter 3. details the comparison of the ER trajectory reconstruction methods. Chapter 4 discusses the conclusions drawn from this work.

Chapter 2

Hardware Work

The hardware portion of this project was performed at LANSCE in collaboration with the Weak Interactions group. The goal of work was to develop a charge readout for use with a negative-ion GEM TPC for a MIGDAL Phase II experiment to probe the low energy regime of the Migdal effect. The Phase II detector has a similar setup to the current MIGDAL detector but instead of a camera readout it has 2D (xy) strips that read out charge.

LANSCE currently houses the DAQ for the Mini-CAPTAIN liquid argon TPC. The goal of the Cryogenic Apparatus for Precision Tests of Argon Interactions with Neutrinos (CAPTAIN) project was to increase understanding of operating large volume liquid argon TPCs. Mini-CAPTAIN made the first measurement of high energy neutron interactions in argon [4]. LANSCE also houses a GEM-based TPC from CERN that uses 2D strips to readout charge. The goal of the project at LANSCE was to instrument the strip readout with the Mini-CAPTAIN electronics and modify the DAQ software to work with the new MIGDAL TPC.


Figure 2.1: Mini-CAPTAIN DAQ

At LANSCE work was done on reducing base noise for the test detector and characterizing the readout noise of the DAQ. The initial noise was greater than 1 V peak-to-peak, too high to detect any physical events. To reduce this base noise to the scale of ~ 100 mV so it was possible to detect real events from cosmic rays or background radioactivity, shielding was built to house the

7

detector. The detector was covered with a Faraday cage constructed using copper mesh, and the whole setup was placed on a custom-built table (Fig 2.2a). Reducing the noise would then allow us to connect the detector to the mini-CAPTAIN electronics and start debugging the full system.

The detector was constructed from a CERN triple-GEM detector kit. It had a wire mesh cathode, that high-voltage could be applied across, then a 2.5 mm drift gap to the top of GEM 1. Between each GEM there was a 2 mm transfer gap, and a 1.5 mm induction gap between the bottom of GEM 3 and the strip readout. The strip readout was not used during these tests to avoid introducing uncertainty in the source of noise, whether noise was from the detector or DAQ. GEMs are a composite sheet consisting of a substrate, an insulator, and two thin conducting sheets, in this case copper, on either side of the substrate with a grid of holes through the whole sheet [2]. They operate through a voltage differential between the top and bottom surfaces that generates a strong electric field. Charge that drifts through a GEM undergoes avalanche gain, multiplying the initial charge for easier detection. While the detector operated a 75:25 $Ar:CO_2$ gas mixture flowed through it. The GEM signals were read out through an ORTEC 142 preamplifier and a Teledyne T3DSO2000A series digital oscilloscope.
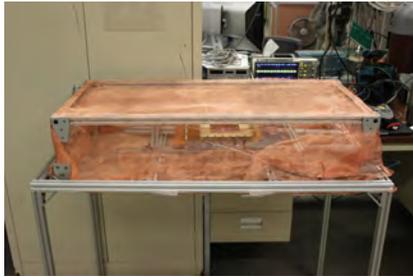
(a) Detector on the table built for it, with the Faraday cage over it.
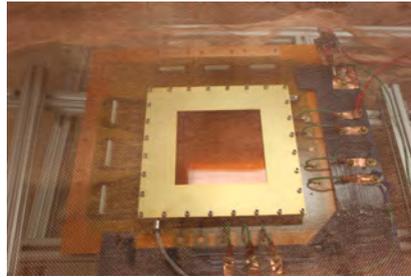
(b) Close up of the detector under the Faraday cage.

Figure 2.2

Several different voltage divider schemes were tested to characterize the output signals of the detector and ensure the required voltage differential across the GEMs. Depending on the divider scheme, one or two high-voltage power supplies were utilized to apply a voltage differential across the GEMs. Depending on the voltage divider setup, readout was either off the ground of the detector, the bottom of GEM 3, or the top of GEM 3.

The initial detector setup had negative high voltage input to the cathode with the voltage divider scheme shown in Fig 2.3a. The next divider scheme disconnected the bottom of GEM 3 from ground to read off through the preamplifier and oscilloscope. The setup that was most extensively tested used the top of GEM 3 for readout both with and without positive high-voltage biased through the pre-amplifier. This is shown in Fig 2.4a. The final divider configu-
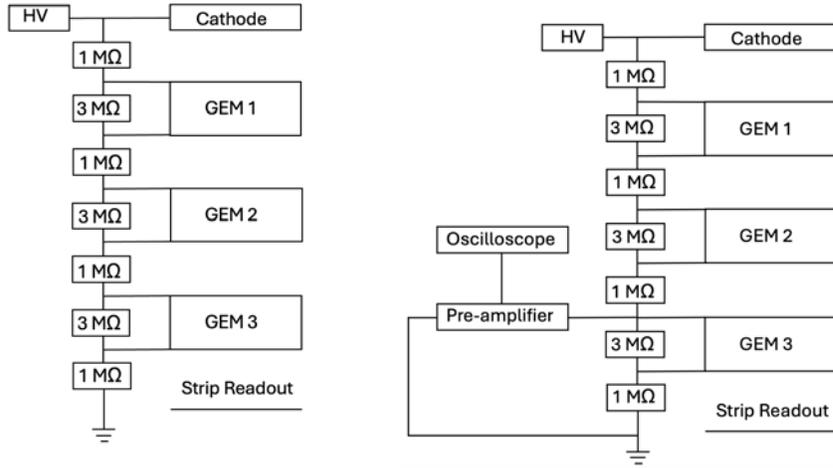
(a) Original voltage divider set up.   (b) Second voltage divider set up.

Figure 2.3

ration tested had the bottom of GEM 2 connected to ground and readout from the top of GEM 3. Noise tests were conducted in all divider set ups; shielding various components and slowly raising the voltage input to the detector.

After considerable effort to find and eliminate sources of electronics noise, it had been reduced to ~ 30 mV peak-to-peak, low enough to detect events, Fig 2.6. The final measurements were done using the final divider setup shown in Fig 2.3b. Raising the GEM voltages to the point where gas amplification is expected in the 1 atmosphere 70:30 $Ar:CO_2$ gas mixture, 1 potential background event was recorded, either a cosmic ray or from radioactivity. This is shown in Fig 2.6. Unfortunately, this was also the last week work was being conducted, so we were unable to collect more data to verify this event.
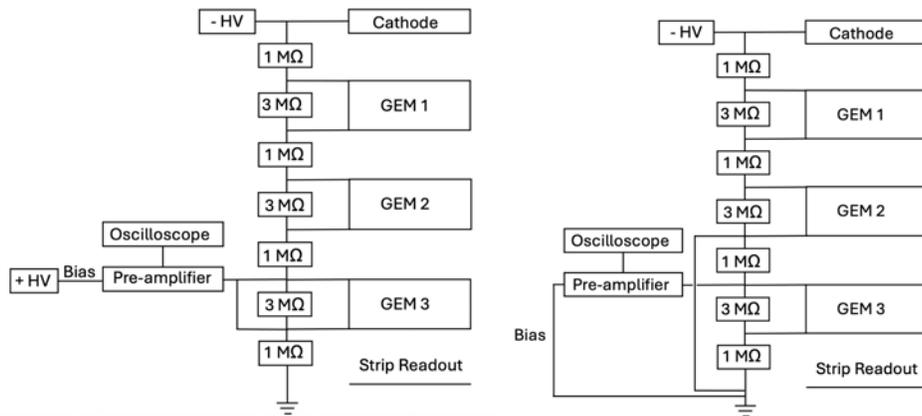
(a) Voltage divider set up tested most extensively. Positive high-voltage was biased through the pre-amplifier to the top of GEM 3.

(b) Final Voltage divider set up. Detector configuration when potential event was detected.
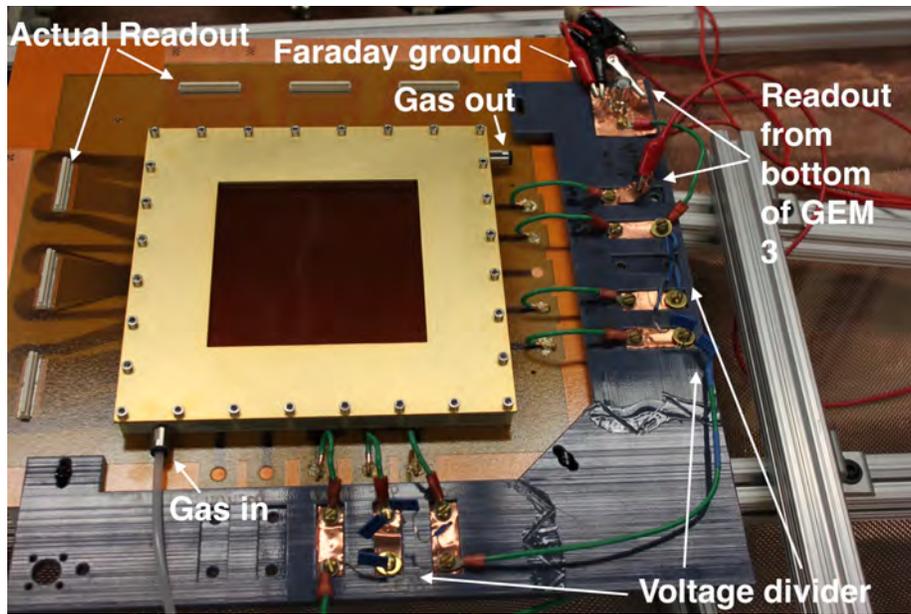
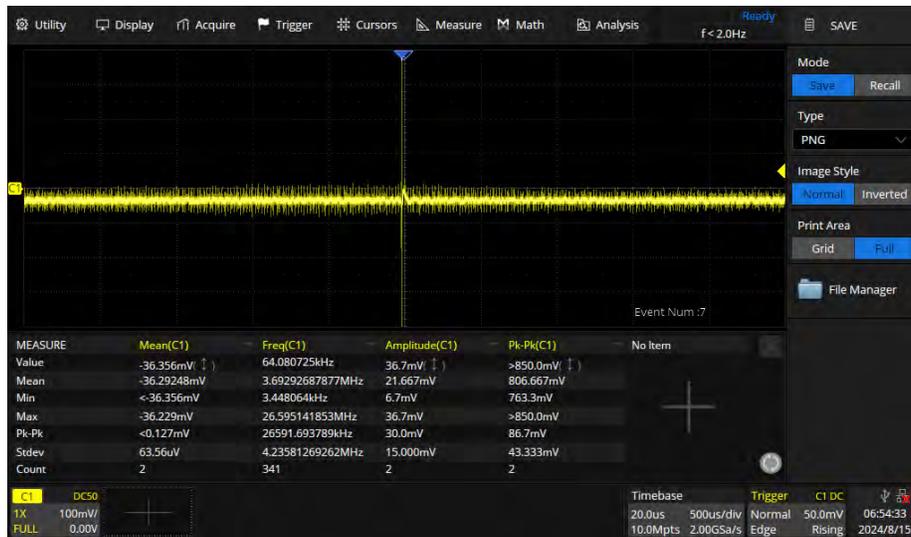Figure 2.4

Figure 2.5: Image of detector in divider set up 2.

Figure 2.6: Potential event recorded on the test detector. This was in the two GEM setup with 1050 V total,

Chapter 3

Software Work

This section will discuss the work on developing and testing algorithms for directional reconstruction of ER tracks. Two reconstruction algorithms were evaluated and quantitatively compared. A novel application of machine learning using the Ultralytics YOLOv8m-pose (YOLO) neural network, and a reconstruction of a moment analysis based algorithm used by the IXPE collaboration to analyze X-ray photoelectrons. The analysis is performed on 2D projections of simulated 3D ER tracks. These methods are evaluated on two criteria: vertex distance and angular resolution. Vertex distance is the mean distance between the true vertex and the reconstructed vertex. Angular resolution is the mean angle of the distribution of angles between the true direction and the reconstructed direction. This work uses ERs simulated to the specifications of the MIGDAL TPC. Primary electron tracks are generated in DEGRAD (public software developed by CERN used to simulate electron tracks) at 5.9 keV in 50 torr of CF_4 with drift, diffusion, and gain added representative of the MIGDAL TPC. The outputs are then digitized according to the output of the OQC used by MIGDAL for optical readout. Only single event ERs that were fully contained within the detection volume were used.


(a) Object detection   (b) Keypoint detection

3.1 YOLO

Deep learning-based object detection is a modern computer vision application where an algorithm is trained to simultaneously classify and localize any number of objects in image data. Convolutional neural network-based object detection algorithms similar to YOLO have broad applications outside of physics but have also proven helpful for high energy physics applications such as the MIGDAL experiment's search for the Migdal effect [7]. Part of the motivation to implement YOLO was its out-of-the-box support of simultaneous object and keypoint detection. Keypoint detection goes a step further than object detection; it detects predefined keypoints in addition to detecting objects with bounding boxes. Crucially, the sets of points that keypoint detection algorithms evaluate are of fixed length and ordered which offers an opportunity for directional reconstruction of track trajectories. In this application, YOLO is trained to identify the first two primary ionization points of a simulated ER assuming a perfect signal-to-noise ratio and no noise. YOLO performs supervised learning, meaning it is trained on images labeled with the bounding box and keypoint coordinates, and event classification. The coordinates of the bounding box are the center, width, and height of the box, and the keypoint coordinates are the first and second primary ionization points of the primary track.

	Train	Test	Validate	Evaluation
Number of Events	70690	8837	8836	58778

Table 3.1: Dataset partitioning for ML training and evaluation
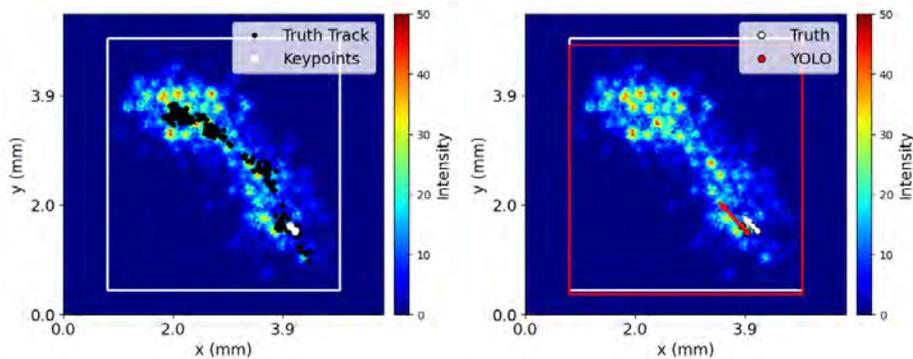
(a) Image of an ER event, the true electron track is in black. The bounding box and first two primary ionization points are in white.

(b) Image of YOLOs predictions for an event in red and the truth in white

Figure 3.2

YOLO returns its predictions in the same format it is trained. This allows it

13

to simultaneously predict the location of the vertex and direction of the track. The first predicted point is the vertex, and the second is used with the vertex to determine the direction of the track. To maintain event structure and increase dynamic range to include more energetic events, the images are set to a log scale. An early stopping criterion was defined such that if there was no improvement in the mAP@50:95:5 metric [11] over 25 successive training epochs, training was stopped. A vector is defined using the first two ionization points of the primary ionization distribution to approximate the best possible 2D angular resolution. This was used to characterize the angular performance of both YOLO and the moment analysis reconstruction.

3.2 Moment Analysis Reconstruction

To quantitatively compare YOLO's results with existing electron directional reconstruction methods, we recreated a moment-based analysis algorithm used to analyze astrophysical X-ray polarimetry data from the IXPE experiment [3][9].

The moment analysis reconstruction is based on the determination of orthogonal principal axes for the distribution of charge. The length of these axes define the major and minor principal axes of a weighted ellipse fit to each track. The initial coordinates x_i, y_i, q_i, are the xy coordinates of each pixel that collected charge, and q the intensity of that charge. The barycenter of the charge distribution, shown in Fig 3.5 (a), is calculated through the first moment, Eq 3.1, and is fixed as the origin of the coordinate system through a translation, $x_i \rightarrow x_i - x_b$, $y_i \rightarrow y_i - y_b$. It is the charge-weighted mean of the distribution.

$$
\begin{aligned}
x_b &= \frac{\Sigma_i q_i x_i}{\Sigma_i q_i} \\
y_b &= \frac{\Sigma_i q_i y_i}{\Sigma_i q_i},
\end{aligned}
\tag{3.1}
$$

The second moment, the variance, of the charge distribution can be calculated along an arbitrary angle ϕ with respect to the x-axis.

$$
M_2(\phi) = \frac{\Sigma_i q_i x_i'^2(\phi)}{\Sigma_i q_i} = \frac{\Sigma_i q_i (x_i \cos \phi + y_i \sin \phi)^2}{\Sigma_i q_i}
\tag{3.2}
$$

Imposing:

$$
\frac{\partial M_2(\phi)}{\partial \phi} = 0
\tag{3.3}
$$

allows for two values of ϕ, in the interval $[-\pi, \pi]$, to be found.

$$
\phi_{max,min} = -\frac{1}{2} \tan^{-1} \left[\frac{2\Sigma_i q_i x_i y_i}{\Sigma_i q_i (y_i^2 - x_i^2)} \right]
\tag{3.4}
$$

14

These maximize and minimize Eq 3.2. As such ϕ_{max} and ϕ_{min} define the angle of rotation, from the x-axis, of the the major and minor principal axes of the weighted ellipse. $\sqrt{M_2(\phi_{max})}$ defines the length of the major axis of the ellipse. The eccentricity e of the ellipse can be expressed as ϵ the ratio of M_2^{max} and M_2^{min}.

$$\epsilon = \frac{M_2^{max}}{M_2^{min}} = \frac{1}{\sqrt{1-e}} \tag{3.5}$$

The third moment, the skewness, is used to determine on which side of the barycenter the Bragg peak lies, whether it is positive or negative along the major axis. To create a reconstructed vertex, the direction opposite the Bragg peak is used.

$$M_3 = \frac{\Sigma_i q_i x_i'^3(\phi_{max})}{\Sigma_i q_i} = \frac{\Sigma_i q_i (x_i \cos\phi_{max} + y_i \sin\phi_{max})^3}{\Sigma_i q_i} \tag{3.6}$$

A function of ϵ and $\sqrt{M_2(\phi_{max})}$ is used to determine how far along the major principal axis the reconstructed vertex should be.

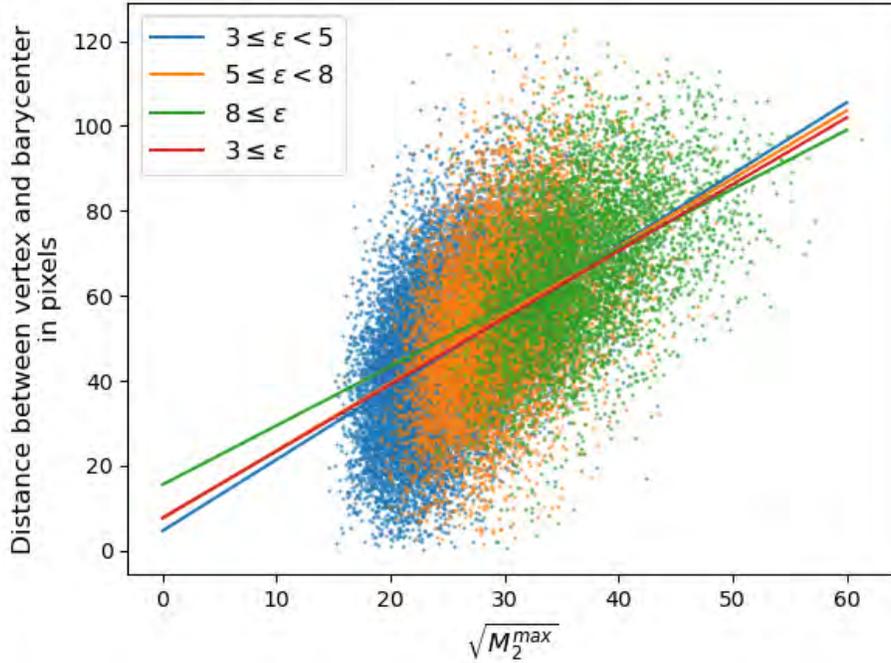$$d = f(\epsilon)\sqrt{M_2^{max}} \tag{3.7}$$

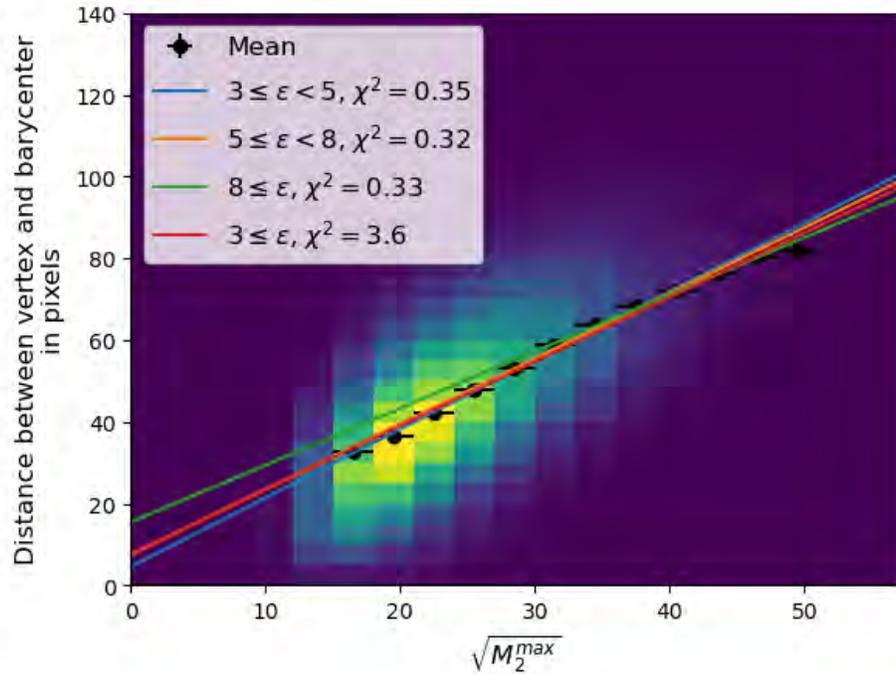Figure 3.3: Linear fits to distribution of vertex to barycenter distance and ellipse major axis length

Figure 3.4: 2D histogram of distances between vertex and barycenter and ellipse major axis length. The black points show the mean distance between vertex and barycenter for each bin.

Three linear functions, $f_j(\epsilon)$; $j \in \{1, 2, 3\}$, were determined by performing first order polynomial fits to the distribution of distances between the vertex and the barycenter against the length of the major axis of the ellipses. Higher order polynomial fits had reduced χ^2 values that suggested extreme overfitting of the data. As such, we chose linear fits for separate domains. Despite the reduced χ^2 for the linear fits remaining below unity we opted to use them to reduce free parameters. To ensure better fits, three domains of ϵ were defined and fits were performed separately on each domain. $f_1(\epsilon)$ is fit for events with $3 \leq \epsilon < 5$, $f_2(\epsilon)$ for events with $5 \leq \epsilon < 8$, and $f_3(\epsilon)$ for events with $8 \leq \epsilon$. A cut is defined so only events with $\epsilon > 3$ were evaluated, these are events that are more eccentric. Events with low eccentricity are more circular and thus it is more difficult to extract directional information from them. However, this cut does introduce a significant efficiency loss. This cut was introduced by the IXPE collaboration to ensure that the algorithm was was being applied to optimal tracks, so we have chosen to carry that over to this analysis.

After a reconstructed vertex is found, the analysis is performed again to find a second reconstructed vertex and attempt to determine angular orientation. The second moment analysis begins by defining a horseshoe region around the
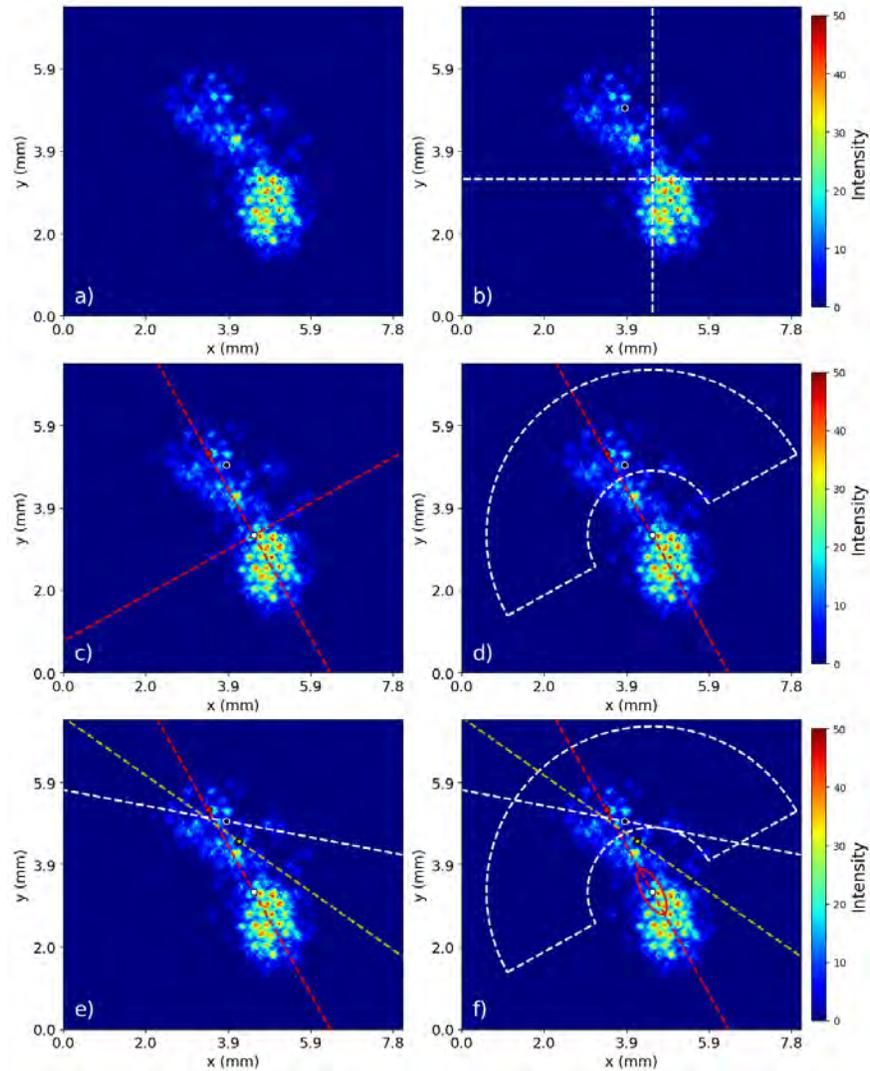
16

Figure 3.5: a) Image of an ER event. b) Barycenter of the track as the origin with the truth vertex. c) The major and minor principal axes with the first reconstructed vertex in red, true vertex in black, and barycenter in white. d) The horseshoe region where the second moment analysis is performed. e) The major principal axes and reconstructed vertices from both moment analyses, 1st in red and 2nd in yellow. The true vertex is black and the white line is the true direction. f) The horseshoe region where the second moment analysis is performed. The weighted ellipse that is defined by the length of the major and minor principal axes in red. The major principal axes and reconstructed vertices from both moment analyses, 1st in red and 2nd in yellow. The true vertex in black and the true direction in white. Shows all previous steps and ellipse.
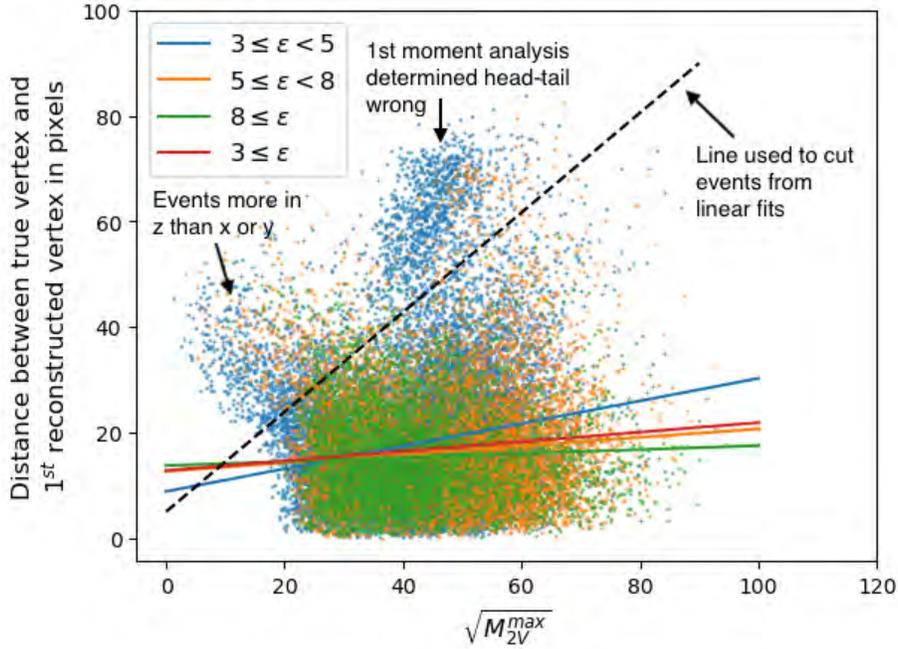
Figure 3.6: Linear fits to distribution of vertex to reconstructed vertex distance and ellipse major axis length for the second moment analysis as well as the events that were cut when performing the fits. These events were still fully analyzed.

barycenter containing the reconstructed vertex. Only charge that falls within that region is considered for the rest of the analysis. This charge is additionally weighted by $w = e^{-\frac{d}{w_0}}$ where d is the distance from the vertex and w_0 is 0.1. w_0 was chosen to significantly weight the pixels, but maintain more statistics. At smaller w_0 values a substantial number of the events would drop out.

The first reconstructed vertex is treated as the barycenter, coordinates are translated so it is the origin. Then the second and third moments are calculated. New fits are determined similarly to the first fits. The same three domains of ϵ were defined and fits were performed on the distribution of distances between the first reconstructed vertex and the true vertex, and the lengths of the major axis of the ellipse formed during the second moment analysis. A number of events were cut out when performing the fits, events that the first moment analysis had determined the wrong direction along the major axis and events that were more in the z extent than x or y. These events were only cut for the purpose of determining the distance along the major axis of the second moment analysis; they were still put through the complete analysis and are reported in the results. Linear fits were chosen again to reduce the number of free parameters and to remain consistent in polynomial degree across all ϵ domains. The angle of
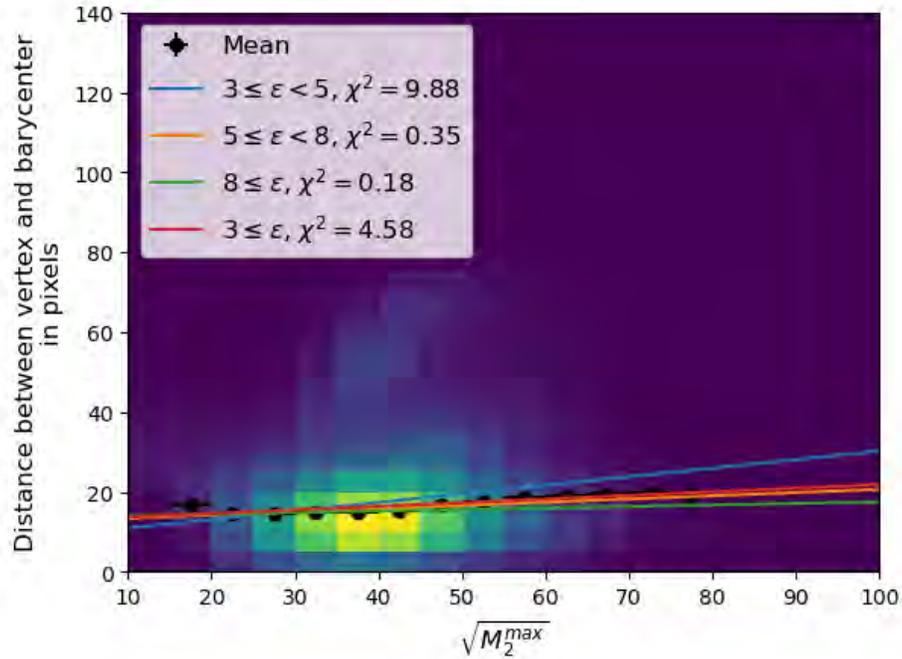
Figure 3.7: 2D histogram of distances between vertex and reconstructed vertex and ellipse major axis length for the second moment analysis. The black points show the mean distance between vertex and reconstructed vertex for each bin.

the first major principal axis is considered the reconstructed electron direction. Angular resolution is determined by finding the angle between the reconstructed electron direction and the truth direction from DEGRAD.

3.3 Results

Results were quantified by comparing vertex distance and angular resolution between YOLO and the IXPE algorithm. We define vertex distance as the Euclidean distance between the reconstructed vertex and the first primary ionization point of the simulated track, the truth vertex. Angular resolution is defined as the mean of the distribution of angles between the true initial direction of the ER and the reconstructed direction. A truth angular resolution was also calculated using the vector created by the first two primary ionization points as the reconstructed direction. We define this vector to represent the best reconstruction of the electron direction.

The results of this analysis are listed in Table 3.2. YOLO was additionally evaluated separately on the same subset of the dataset the moment analysis
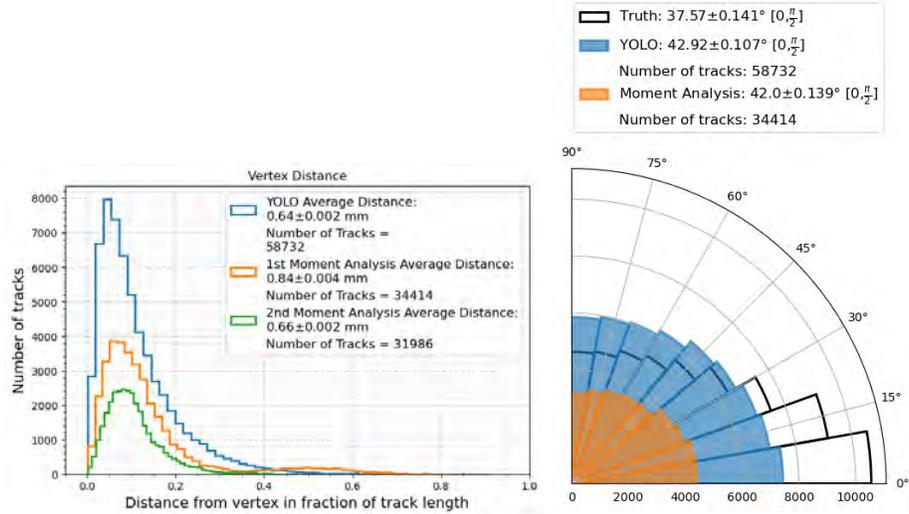
(a) Vertex distances for YOLO, the 1st moment analysis, and the 2nd moment analysis

(b) Distribution of angles between the reconstructed track axis and true axis for YOLO and the 1st moment analysis. The truth distribution is the angle between the true electron direction and the vector formed from the first two primary ionization points.

Figure 3.8

was fully performed on, events with $\epsilon > 3$. Overall, YOLO performed best on vertex placement, performing better than either moment analysis on the same subset of the dataset and better on the whole dataset. We ignore head-tail in our evaluation of angular resolution, which restricts the angle between the reconstructed and truth axis of a track to the domain of $[0°, 90°]$ with $45°$ – the angle between two random axes on a plane – being the limit of no angular resolution. Overall, we found the first moment analysis to slightly outperform both YOLO and the second moment analysis in angular resolution, however all of these methods performed similarly and were hardly better than random chance. Given that we achieve an average angular resolution of 37.6 degrees with knowledge of the truth-simulated primary track, there is room for improvement in our algorithmic angular reconstructions.
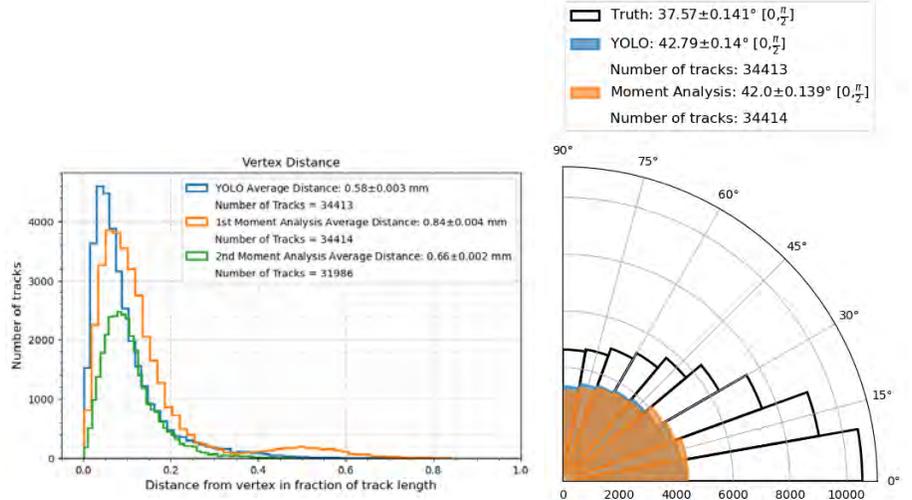
(a) Vertex distances for YOLO and both moment analyses on the subset of tracks with $\epsilon > 3$

(b) Distribution of angles between the reconstructed track axis and true axis for YOLO and the 1st moment analysis on the subset of events with $\epsilon > 3$. The truth distribution is the same as in Fig 3.8b.

Figure 3.9

Analysis Method	% of Dataset	Mean Vertex Distance (mm)	Mean Angular Resolution
YOLO	100	0.64 ± 0.002	$42.9 \pm 0.11°$
YOLO ($\epsilon > 3$ cut)	58.6	0.58 ± 0.003	$42.7 \pm 0.14°$
1st Moment Analysis	58.6	0.84 ± 0.004	$42.0 \pm 0.14°$
2nd Moment Analysis	54.4	0.66 ± 0.002	$42.3 \pm 0.14°$

Table 3.2: Analysis results for each method. The uncertainty on each measurement is the standard error of the mean.

Chapter 4

Conclusion

Many experiments require electron directionality for a wide range of applications, especially those that involve rare event searches. In particular, it can be used to verify the origin of a signal, remove backgrounds, or confirm event topologies. The IXPE collaboration currently uses electron directionality to determine the polarization of ionizing X-rays from astrophysical sources. Reconstructing electron trajectory is also essential for validating the topology of rare events such as from $0\nu\beta\beta$ or the Migdal effect. As stated before, ERs have complicated trajectories similar to a random walk. Therefore, reconstructing their initial direction can only be done at the start of their tracks, i.e. the interaction vertex. Two methods of vertex reconstruction were evaluated here.

Novel ML methods of ER vertex reconstruction are viable. For the dataset tested here, YOLO had better overall performance on vertex placement and particularly the subset that the moment analysis performed best on. Both methods were on par for angular resolution. The first moment analysis performed best at determining a reconstructed direction, but there was a significant efficiency loss. At this electron energy, YOLO shows promise and has results comparable to moment analysis event reconstruction. We are excited to continue this work by comparing YOLO's capacity at multiple electron energies and to test the performance of an additional event topology-based track fitting algorithm. These results have wide-ranging applications and introducing more energies may broaden their apparent implications..

Acknowledgments

I would like to thank Professor Dinesh Loomba and Dr. Jeffrey Schueler for their support and guidance throughout my work on this project. I am also grateful to Dr. Steve Elliott and Dr. Ralph Masssarczyk at LANSCE for their instruction and help while I conducted work over the summer. I would also like to thank Mark Flynn for helping me when I ran into coding issues.

Bibliography

[1] R. Bellazzini and F. Muleri. X-ray polarimetry: A new window on the high energy sky. *Nuclear Instruments and Methods in Physics Research Section A: Accelerators, Spectrometers, Detectors and Associated Equipment*, 623(2):766–770, 2010. 1rs International Conference on Frontiers in Diagnostics Technologies.

[2] R. Bouclier, M. Capeans, W. Dominik, M. Hoch, J.-C. Labbe, G. Million, L. Ropelewski, F. Sauli, and A. Sharma. The gas electron multiplier (gem). *IEEE Transactions on Nuclear Science*, 44(3):646–650, 1997.

[3] A. Di Marco et al. A weighted analysis to improve the x-ray polarization sensitivity of the imaging x-ray polarimetry explorer. *The Astronomical Journal*, 163:170, 04 2022.

[4] C.E. Taylor et al. The mini-captain liquid argon time projection chamber. *Nuclear Instruments and Methods in Physics Research Section A: Accelerators, Spectrometers, Detectors and Associated Equipment*, 1001:165131, 2021.

[5] E. Costa et al. An efficient photoelectric x-ray polarimeter for the study of black holes and neutron stars. *Nature*, 2001.

[6] H.M. Araújo et al. The migdal experiment: Measuring a rare atomic process to aid the search for dark matter. *Astroparticle Physics*, 151:102853, 2023.

[7] J. Schueler et al. Transforming a rare event search into a not-so-rare event search in real-time with deep learning-based object detection. *Phys. Rev. D*, 111:072004, Apr 2025.

[8] L. Baldini et al. Design, construction, and test of the gas pixel detectors for the ixpe mission. *Astroparticle Physics*, 133:102628, 2021.

[9] R. Bellazzini et al. Novel gaseous x-ray polarimeter: data analysis and simulation. In Silvano Fineschi, editor, *Polarimetry in Astronomy*, volume 4843, pages 383 – 393. International Society for Optics and Photonics, SPIE, 2003.

[10] A. Migdal. Ionizatsiya atomov pri yadernykh reaktsiyakh (Ionization of atoms in nuclear reactions). *ZhETF*, 9:1163–1165, 1939.

[11] Rafael Padilla, Sergio Netto, and Eduardo da Silva. A survey on performance metrics for object-detection algorithms. 07 2020.